Volume 61
Number 18
4 March 2025
Pages 3571–3766

ChemComm

Chemical Communications

rsc.li/chemcomm

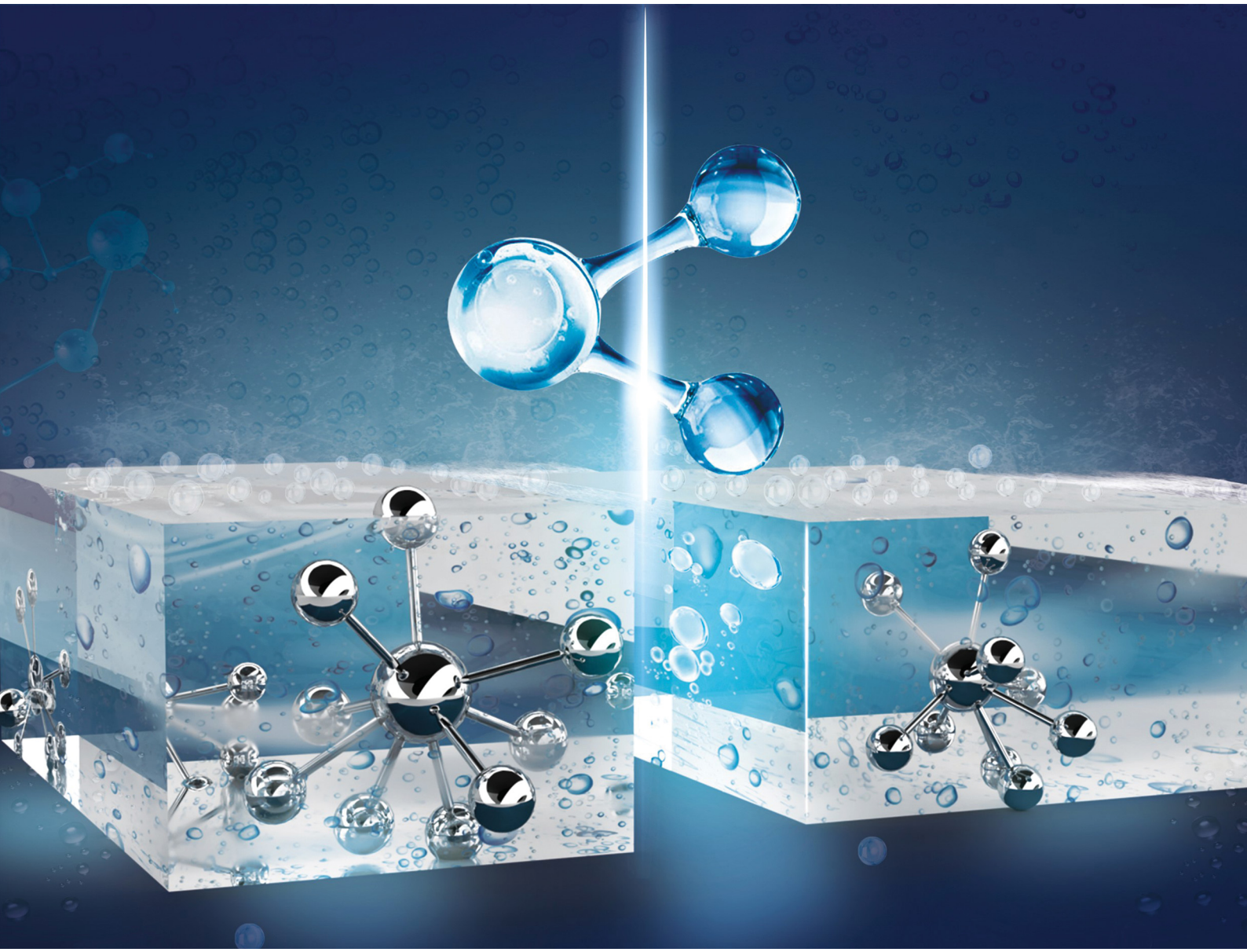

ISSN 1359-7345

ROYAL SOCIETY OF CHEMISTRY

COMMUNICATION

Dengsong Zhang, Juntao Huo, Guowei Li *et al.*
Interfacial creation of positively charged sites in $LaPO_4/Fe_3(PO_4)_2$ heterojunctions for high-current-density oxygen evolution

Published on 25 January 2025. Downloaded by Ningbo Institute of Materials Technology and Engineering, CAS on 12/17/2025 9:55:19 AM.

ChemComm

ROYAL SOCIETY OF CHEMISTRY

COMMUNICATION

View Article Online
View Journal | View Issue

Check for updates

Cite this: *Chem. Commun.*, 2025, **61**, 3669

Received 2nd January 2025,
Accepted 24th January 2025

DOI: 10.1039/d5cc00018a

rsc.li/chemcomm

Interfacial creation of positively charged sites in $LaPO_4/Fe_3(PO_4)_2$ heterojunctions for high-current-density oxygen evolution†

Sitong Liu,[ab] Yudi Zhang,[bc] Wen Sun,[bc] Junqiang Wang,[bc] Dengsong Zhang,*[a] Juntao Huo*[bc] and Guowei Li*[bc]

The creation of positively charged active sites is crucial for enhancing the adsorption of negatively charged hydroxide ions, thereby improving the sluggish oxygen evolution reaction (OER). We engineered $LaPO_4/Fe_3(PO_4)_2$ heterojunctions with a low flat-band potential, facilitating interfacial charge transfer and generation of positively charged holes, resulting in a highly active and stable OER catalyst at 500 mA cm^{-2}.

The development of highly active catalysts is crucial for the advancement of energy conversion technologies, particularly in the field of electrocatalytic water oxidation involving multiple electron transfers and reaction intermediates.[1–3] For the purpose of working actively and stably under high industrial current densities, the electron structures at the local active sites should be modulated for the enhanced adsorption of OH^-, thus lowering the energy barriers of the crucial rate-determination step.[4–6] This can be achieved by designing catalysts with unique functional sites that lower the reaction energy barrier and optimize adsorption/desorption behaviors, such as by elevating the oxygen 2p energy level.[7] Among the various strategies to enhance catalytic performance, the engineering of heterojunctions is particularly noteworthy due to its capacity to optimize charge transfer and increase the number of active sites.[8–10] In heterojunctions, the combination of materials with distinct electronic structures can offer many advantages, such as promoting favorable charge redistribution, increasing the availability of active sites, and enhancing catalytic activity by facilitating efficient charge transfer.[11,12] The interface in heterojunctions often leads to a redistribution of charge, where the electronic states of one material can influence the charge distribution of the adjacent material. Such a redistribution at the interface will facilitate the water dissociation and adjusting the binding strength of adsorbed intermediates, thus accelerating OER kinetics at large current density.[11] Interestingly, an internal electric field can be created at the interface that drives the separation of photoinduced or electrochemically generated charges. This improves the transport of charge carriers to the catalytic sites.[13,14] The synergy between the different materials in a heterojunction can also lead to the creation of more active sites for the OER.[7,15,16] For instance, one material may provide abundant active sites for the adsorption of hydroxide ions, while the other may improve electronic conductivity or act as a co-catalyst.[17] However, despite the numerous benefits, constructing heterojunctions for OER catalysts still faces various challenges, such as achieving optimal material combinations, and controlling interface structures remains a challenge. Thus, it is urgent to develop an effective strategy to construct phase interfaces that exhibit strong interfacial interactions, which can accelerate mass transport and kinetics,[18] and maintain stability at industrial-scale current densities.[19,20]

Transition–metal phosphates have emerged as promising non-precious metal electrocatalysts due to their low cost, structural stability, and distinctive physicochemical properties.[21,22] These phosphates, composed of metal centers and phosphate groups, form open-framework layered structures that facilitate proton conductivity,[23] facilitating efficient OER catalysis. Phosphate cobalt has been reported as an efficient OER electrocatalyst in neutral solutions, with the phosphate group acting as a proton acceptor, thereby improving the system's stability.[24] The incorporation of PO_4^{3-} into amorphous $FePO_4$ could alter the electronic structure, lowering the d-band center and weakening the binding strength of key

[a] *State Key Laboratory of Advanced Special Steel, School of Materials Science and Engineering, International Joint Laboratory of Catalytic Chemistry, College of Sciences, Shanghai University, Shanghai 200444, China. E-mail: dszhang@shu.edu.cn*
[b] *CAS Key Laboratory of Magnetic Materials and Devices, Ningbo Institute of Materials Technology and Engineering, Chinese Academy of Sciences, Ningbo 315201, China. E-mail: huojuntao@nimte.ac.cn, liguowei@nimte.ac.cn*
[c] *Center of Materials Science and Optoelectronics Engineering, University of Chinese Academy of Sciences, Beijing 100049, China*

† Electronic supplementary information (ESI) available. See DOI: https://doi.org/10.1039/d5cc00018a

Published on 25 January 2025. Downloaded by Ningbo Institute of Materials Technology and Engineering, CAS on 12/17/2025 9:55:19 AM.

intermediates, thus promoting oxygen release.[25] Moreover, surface reconstruction induced by the pyrophosphate ligand under harsh OER conditions has been shown to result in highly distorted tetrahedral geometries. These distorted structures are more favorable for the adsorption of water molecules, which in turn optimizes the local coordination environment of transition metal centers. This enhancement accelerates the OER kinetics by improving the efficiency of water adsorption and facilitating the reaction process.[21,26] Given these facts, the development of a novel, more efficient electrocatalyst based on heterostructures is particularly crucial.

In this research, we introduce a large-radius rare earth element to construct a rare earth-transition metal heterostructure, with the purpose of guiding the design and selection of high-performance, stable alkaline water electrolysis catalysts. The incorporation of lanthanum (La) induces lattice distortion, creating a strain effect that facilitates the tuning of the electronic structure.[27] The synthesized $LaPO_4/Fe_3(PO_4)_2$ catalyst exhibited a low overpotential of 210 mV at 10 mA cm^{-2}. It demonstrated exceptional stability, maintaining high performance at 500 mA cm^{-2} for 380 hours without significant degradation.

For the synthesis of metal phosphate heterojunctions, nickel foam (NF) was first impregnated in a solution containing the respective metal precursors (Fig. 1a, details see ESI†). A thin layer of black deposits was successfully formed on the surface of the nickel foam after thorough washing. X-ray diffraction (XRD) confirms the existence of two phases (Fig. 1b). The successful fabrication of the composite material $LaPO_4/Fe_3(PO_4)_2$ was achieved through the effective integration of components $LaPO_4$ and $Fe_3(PO_4)_2$. The main peaks of $LaPO_4$ align well with the monoclinic phase of lanthanum phosphate, whereas the peaks for $Fe_3(PO_4)_2$ align with the monoclinic phase of iron phosphate (Fig. S1, ESI†).[28] The scanning electron microscopy (SEM) image demonstrates that the catalyst was uniformly distributed on the three-dimensional porous structure of the nickel foam substrate, exhibiting a smooth surface without visible cracks (Fig. 1c). Energy dispersive spectroscopy mapping of the $LaPO_4$ and $Fe_3(PO_4)_2$ powders (Fig. S2, ESI†) confirmed that La, O, P, and Fe were uniformly distributed. Transmission electron microscopy was employed to further uncover the phase compositions (Fig. 1d). The lattice fringes with a measured distance of 0.295 nm are aligned with the (111) planes of $LaPO_4$, which is further supported by the corresponding fast Fourier transform (FFT) patterns (Fig. S3a, ESI†). The lattice spacing of 0.317 nm can be indexed to the (211) planes of $Fe_3(PO_4)_2$ (Fig. S3b, ESI†). The heterointerface regions are distinctly visible in Fig. 1d, highlighting the close interaction between $LaPO_4$ and $Fe_3(PO_4)_2$.

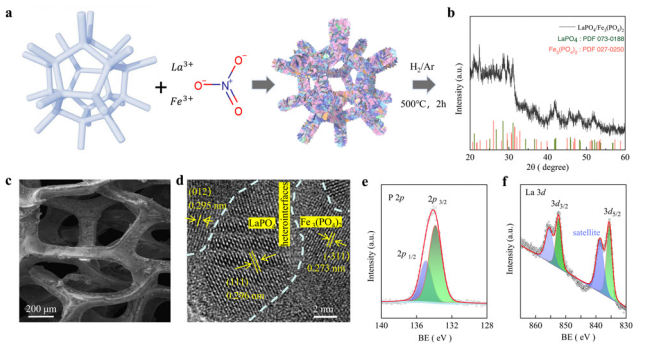

Fig. 1 (a) Schematic illustration of the synthesis of $LaPO_4/Fe_3(PO_4)_2$. (b) XRD patterns of the composite catalyst. (c) SEM and (d) HRTEM of the catalyst. XPS spectra of (e) La 3d, and (f) Fe 2p.

X-ray photoelectron spectroscopy (XPS) measurements were conducted to investigate the electronic interactions within the catalyst. The XPS survey spectrum (Fig. S4a, ESI†) distinctly reveals characteristic peaks of the expected elements. Specifically, the peaks at 133.8 eV and 134.7 eV in the high-resolution XPS spectra of P 2p correspond to the PO_4^{3-} group (Fig. 1e).[29] In the La 3d region (Fig. 1f), two principal peaks at 835.6 eV and 852.4 eV represent La $3d_{5/2}$ and La $3d_{3/2}$, respectively. Additional peaks at 855.5 eV and 838.7 eV are indexed to the corresponding satellite peaks, confirming their attribution to the $LaPO_4$ phase.[29] The Fe 2p spectrum (Fig. S4c, ESI†) reveals the presence of both Fe^{2+} and Fe^{3+} within $Fe_3(PO_4)_2$.[30]

The OER performance of the heterostructure is investigated under a three-electrode electrocatalysis setup. The OER activity of the nickel foam is included to ensure that its contribution is negligible. We also prepared a series of composites with varying La : Fe ratios and tested their electrochemical properties. The composites with a La : Fe ratio of 1 : 2 demonstrated the best performance, prompting further investigations into their electrochemical properties and the sources of their activity (Fig. S5, ESI†). At a current density of 10 mA cm^{-2}, the overpotential required for $LaPO_4/Fe_3(PO_4)_2$ is 210 mV after ohmic correction (220 mV without *iR* correction, Fig. S5d, ESI†), which is lower than the individual phases of $LaPO_4$ (454 mV), $Fe_3(PO_4)_2$ (231 mV), and commercial RuO_2 (480 mV),[31] highlighting the improved catalytic activity achieved by forming the heterojunction (Fig. 2a). Furthermore, $LaPO_4/Fe_3(PO_4)_2$ maintains this advantage at higher current densities of 100 mA cm^{-2} (Fig. S6, ESI†). The Tafel slope of $LaPO_4/Fe_3(PO_4)_2$ is 35 mV dec^{-1} (Fig. 2b), which is lower than that of commercial RuO_2 (140 mV dec^{-1}), $LaPO_4$ (159 mV dec^{-1}), and $Fe_3(PO_4)_2$ (81 mV dec^{-1}), indicating a faster OER kinetics of the $LaPO_4/Fe_3(PO_4)_2$ catalyst. A Tafel slope of approximately 40 mV dec^{-1} suggests that the rate-determining step in the OER process is the adsorption of hydroxide ions (OH^-) accepting electrons and reacting with water molecules to form oxygen intermediates (O*), which is a common characteristic of OER catalysts.[32,33] The solution resistance obtained from electrochemical impedance spectroscopy is determined to be 0.47 Ω for $LaPO_4/Fe_3(PO_4)_2$, and 1.41 Ω and 0.64 Ω for single-phase catalysts of $LaPO_4$ and $Fe_3(PO_4)_2$ (Fig. S7, ESI†). The lower resistance indicates that the interface formed between the $LaPO_4$ and $Fe_3(PO_4)_2$ heterostructures possesses high electrical conductivity.[34] Through comprehensive comparison of our catalysts with other recently reported metal phosphates and noble metal catalysts, the heterostructures in our work show excellent OER catalytic activity (Fig. 2c). Fig. 2d illustrates the multi-step chronoamperometry of $LaPO_4/Fe_3(PO_4)_2$ at varying current densities ranging from 10 to 1000 mA cm^{-2} without correction. As the

 This journal is © The Royal Society of Chemistry 2025

Published on 25 January 2025. Downloaded by Ningbo Institute of Materials Technology and Engineering, CAS on 12/17/2025 9:55:19 AM.

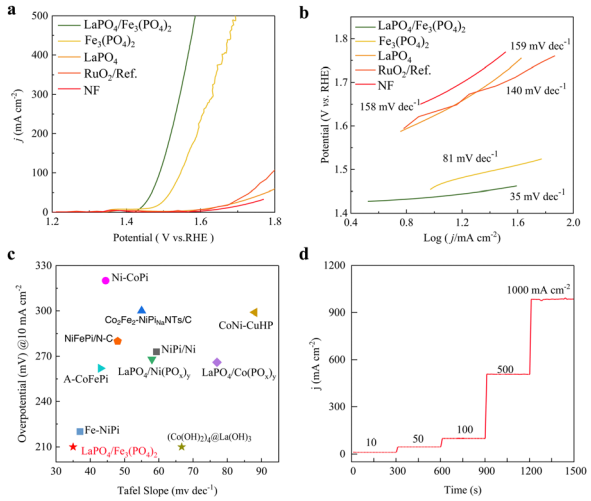

Fig. 2 (a) OER polarization curves of $LaPO_4/Fe_3(PO_4)_2$, $LaPO_4$, $Fe_3(PO_4)_2$, commercial RuO_2 and nickel foam catalysts. (b) The corresponding Tafel slopes. (c) Comparison of the overpotentials and Tafel slopes of the catalyst with those recently reported catalysts at 10 mA cm^{-2}. (d) Multi-current process without *iR* correction of the heterostructure.

overpotential increases, the current density responds accordingly and quickly approaches a relatively stable state, demonstrating a shortened diffusion pathway for OH^- carriers, as well as mechanical stability over a broad range of current densities.[30,35]

Faradaic efficiency is a pivotal parameter for evaluating the performance of catalysts, facilitating the understanding and optimization of energy conversion and mass transformation efficiencies.[36] Utilizing the water displacement method for gas collection (Fig. S8, ESI†), we assessed the faradaic efficiency of the $LaPO_4/Fe_3(PO_4)_2$ catalyst at a current density of 500 mA cm^{-2}. The quantity of oxygen gas produced is in good agreement with theoretical calculations, indicating a nearly 100% faradaic efficiency (Fig. 3a). This result indicates that the catalyst possesses high efficiency and selectivity. Chronopotential measurements were employed to assess the stability of the catalyst at a high current density of 500 mA cm^{-2}. After 380 hours of testing, the overpotential increased by only 12% (Fig. 3b), indicating that the material possesses good electrochemical stability.

Ultimately, we endeavored to uncover the reasons behind the impressive OER performance of the $LaPO_4/Fe_3(PO_4)_2$ heterostructures. The surface structures of the catalysts are

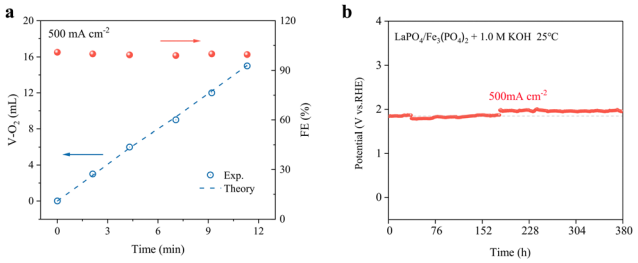

Fig. 3 (a) Faradaic efficiency of the heterostructure at 500 mA cm^{-2}. (b) Long-term stability test at a current density of 500 mA cm^{-2}.

investigated after long-time stability test. SEM images (Fig. S9, ESI†) show a roughened surface on the nickel foam and the formation of cracks. EDS mapping (Fig. S10, ESI†) indicates an increase in the relative content of oxygen and a decrease in phosphorus. TEM images and the corresponding SAED pattern further suggest that the $LaPO_4/Fe_3(PO_4)_2$ heterostructures turn into amorphous (Fig. S11b and c, ESI†), but still keep their metal phosphate phases. This can be proved from the homogeneous elemental distribution (Fig. S12, ESI†) and the existence of the bending mode ($\nu 4$) of the $(PO_4)^{3-}$ group from the Raman spectra (Fig. S13, ESI†).[37]

XPS was conducted to confirm the electron redistribution between the heterostructures. The La 3d spectrum shows a negative shift of 0.3 eV after the OER reaction (Fig. S14c, ESI†), while the Fe 2p peak shifts positively by 0.29 eV to 710.4 eV (Fig. S14d, ESI†). These changes indicate that Fe exhibits a higher oxidation state, which facilitates the formation of highly reactive Fe intermediates by Fe centers with a higher oxidation state during the OER process easily.[38] The high-resolution O 1s spectrum reveals a new oxidation peak at a binding energy of 530.3 eV (Fig. 4a), corresponding to the presence of low-coordinated oxygen species ($O2^-$, O^-, –OH) on the surface.[39] These species facilitate the formation and stabilization of reaction intermediates, thus promoting the water adsorption capability of the $LaPO_4/Fe_3(PO_4)_2$ catalyst.[40]

The Mott–Schottky plot provides invaluable insights into the active sites of catalysts. The negative slope of the Mott–Schottky plot indicates that the main charge carriers of $LaPO_4/Fe_3(PO_4)_2$ are positively charged holes (Fig. 4b). Compared to $Fe_3(PO_4)_2$ (1.68 V) (Fig. S15 and S16, ESI†), the lower flat-band potential of $LaPO_4/Fe_3(PO_4)_2$ (0.85 V) may imply that the conduction band electrons of the catalyst are more easily excited onto the reactant molecules, thus promoting electron transfer, a key step in the OER process. Fig. 4c displays the energy diagram of

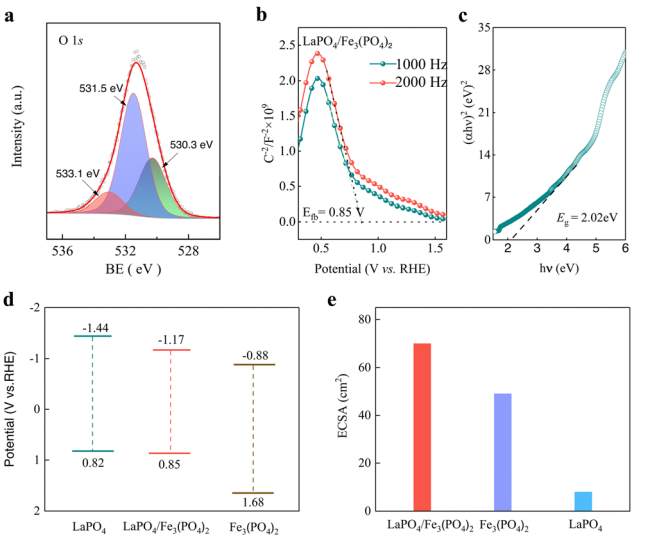

Fig. 4 (a) XPS spectra of O 1s. (b) Mott–Schottky curve of the catalyst measured at 1000 Hz and 2000 Hz. (c) Tauc plots. (d) Band structure diagram and (e) ECSAs of $LaPO_4/Fe_3(PO_4)_2$, $LaPO_4$, and $Fe_3(PO_4)_2$.

Published on 25 January 2025. Downloaded by Ningbo Institute of Materials Technology and Engineering, CAS on 12/17/2025 9:55:19 AM.

these catalysts, where the difference in Fermi levels drives electrons to flow from $Fe_3(PO_4)_2$ to $LaPO_4$ in the $LaPO_4$/$Fe_3(PO_4)_2$ heterostructure, ultimately forming a built-in electric field at the interface. The spontaneous transfer of electrons from $Fe_3(PO_4)_2$ to $LaPO_4$ results in positively charged sites in the $LaPO_4$ phase and electron-deficient sites in $Fe_3(PO_4)_2$. These positively charged sites facilitate the formation of adsorbed intermediates, aiding in the transfer of electrons across the catalyst surface, thereby enhancing the rate of OER. In addition, such an electron redistribution could also produce more active sites for the OER.[41] Therefore, the double-layer capacitance were obtained (Fig. S17, ESI†). The heterostructure exhibited a higher capacitance of 2.8 mF cm^{-2} (Fig. 4d), suggesting a larger number of active sites. These heterojunctions increase active site numbers, optimize electronic structure, and enlarge ECSA, possibly exceeding the sum of individual single-phase materials' ECSAs. Single-phase materials' active sites are limited by intrinsic properties, but heterojunctions overcome this *via* interface engineering and electronic adjustments, providing more effective active sites per unit mass or volume of catalyst.

In conclusion, we have synthesized a $LaPO_4/Fe_3(PO_4)_2$ heterostructure catalyst using the co-precipitation annealing method. The results show that this material possesses low overpotentials and impressive electrochemical stability at high current density. The OER activity of $LaPO_4/Fe_3(PO_4)_2$ is mainly attributed to the formation of positively charged sites as a result of the electron distribution. This electronic modulation contributes to positively charged regions on the $Fe_3(PO_4)_2$ and enhances the OH^- adsorption during the OER, thus leading to a significant reduction in OER overpotential. This provides an easy strategy for modulating the surface charge state of highly efficient electrocatalysts through interfacial engineering, which offers future energy conversion applications.

We acknowledge financial support from the National Natural Science Foundation of China (U24A2039, 52271194, 52222105), the Ningbo Yongjiang Talent Introduction Programme (2022A-090-G), the Hundred Talents Programs in the Chinese Academy of Science, the International Cooperation Project of Ningbo City (2024H007), and the Max Planck Partner Group program.

Data availability

The data supporting this article have been included as part of the ESI.†

Conflicts of interest

There are no conflicts to declare.

Notes and references

1 L. Gao, X. Cui, C. D. Sewell, J. Li and Z. Lin, *Chem. Soc. Rev.*, 2021, **50**, 8428–8469.
2 T. Shuai, Q. Zhan, H. Xu, C. Huang, Z. Zhang and G. Li, *Chem. Commun.*, 2023, **59**, 3968–3999.
3 J. Zhao, K. Yue, H. Zhang, S. Wei, J. Zhu, D. Wang, J. Chen, V. Y. Fominski and G. Li, *Nat. Commun.*, 2024, **15**, 2928.
4 L. Hao, Y. Gao, A. W. Robertson and Z. Sun, *Inno. Mater.*, 2024, **2**, 100050.
5 H. Ma, Y. Jiao, W. Guo, X. Liu, Y. Li and X. Wen, *Innovation*, 2024, **5**, 100571.
6 F. Liu, X. Cai, Y. Tang, W. Liu, Q. Chen, P. Dong, M. Xu, Y. Tan and S. Bao, *Energy Environ. Mater.*, 2024, **7**, e12644.
7 J. Zhao, H. Zhang, C. Li, X. Zhou, J. Wu, F. Zeng, J. Zhang and G. Li, *Energy Environ. Sci.*, 2022, **15**, 3912–3922.
8 K. Villa, *Chem. Commun.*, 2023, **59**, 8375–8383.
9 S. Zheng, H. Xu, H. Zhu, T. Shuai, Q. Zhan, C. Huang and G. Li, *J. Mater. Chem. A*, 2024, **12**, 18832–18865.
10 J. Lai, Z. Zhang, X. Yang and Y. Zhang, *Inno. Mater.*, 2023, **1**, 100020.
11 P. Zhai, C. Wang, Y. Zhao, Y. Zhang, J. Gao, L. Sun and J. Hou, *Nat. Commun.*, 2023, **14**, 1873.
12 Y. Sun, K. Liang, R. Tu, X. Fan, C. Q. Jia, Z. Jia, Y. Li, H. Yang, E. Jiang, H. Liu, Y. Yao and X. Xu, *Energy Environ. Mater.*, 2024, **7**, e12638.
13 Y. Dong, P. Ji, X. Xu, R. Li, Y. Wang, K. P. Homewood, X. Xia, Y. Gao and X. Chen, *Energy Environ. Mater.*, 2024, **7**, e12643.
14 J. He, B. Hu and Y. Zhao, *Adv. Funct. Mater.*, 2016, **26**, 5998–6004.
15 P. Ye, K. Fang, H. Wang, Y. Wang, H. Huang, C. Mo, J. Ning and Y. Hu, *Nat. Commun.*, 2024, **15**, 1012.
16 W. Park, J. Noh, G. H. Gu, G. Nam, S. Jung, Y. Kim and Y. Jung, *Inno. Mater.*, 2024, **2**, 100072.
17 Q. Yang, Y. Zhang, Y. Sun, C. Felser and G. Li, *Inno. Mater.*, 2023, **1**, 100013.
18 X. Xu, Y. Pan, L. Ge, Y. Chen, X. Mao, D. Guan, M. Li, Y. Zhong, Z. Hu, V. K. Peterson, M. Saunders, C. Chen, H. Zhang, R. Ran, A. Du, H. Wang, S. P. Jiang, W. Zhou and Z. Shao, *Small*, 2021, **17**, 2101573.
19 Z. Li, M. Hu, P. Wang, J. Liu, J. Yao and C. Li, *Coord. Chem. Rev.*, 2021, **439**, 213953.
20 J. Tang, X. Xu, T. Tang, Y. Zhong and Z. Shao, *Small Methods*, 2022, **6**, 2201099.
21 S. Yang, K. Yue, X. Liu, S. Li, H. Zheng, Y. Yan, R. Cao and W. Zhang, *Nat. Commun.*, 2024, **15**, 1410.
22 S. Ye, Y. Lei, T. Xu, L. Zheng, Z. Chen, X. Yang, X. Ren, Y. Li, Q. Zhang and J. Liu, *Appl. Catal., B*, 2022, **304**, 120986.
23 X. Li and J. Wang, *Adv. Mater. Interfaces*, 2020, **7**, 2000676.
24 J. Kwon, H. Han, S. Jo, S. Choi, K. Y. Chung, G. Ali, K. Park, U. Paik and T. Song, *Adv. Energy Mater.*, 2021, **11**, 2100624.
25 L. Yang, Z. Guo, J. Huang, Y. Xi, R. Gao, G. Su, W. Wang, L. Cao and B. Dong, *Adv. Mater.*, 2017, **29**, 1704574.
26 H. Kim, J. Park, I. Park, K. Jin, S. E. Jerng, S. H. Kim, K. T. Nam and K. Kang, *Nat. Commun.*, 2015, **6**, 8253.
27 Y. Kang, J. Li, S. Zhang, Y. Xiao, G. Lu and Z. Lei, *ACS Appl. Mater. Interfaces*, 2023, **15**, 55679–55691.
28 A. Wu, H. Bai, J. Bao, K. Yang, L. Feng, Y. Ma, Y. Qiao, W. Li, Y. Liu and X. Zhu, *RSC Adv.*, 2018, **8**, 35813–35818.
29 R. Zhao, Z. Chen, Q. Li, X. Wang, Y. Tang, G. Fu, H. Li, J. Lee and S. Huang, *Chem. Catal.*, 2022, **2**, 3590–3606.
30 G. Li, Q. Yang, J. Rao, C. Fu, S. Liou, G. Auffermann, Y. Sun and C. Felser, *Adv. Funct. Mater.*, 2020, **30**, 1907791.
31 D. Wang, Q. Li, C. Han, Q. Lu, Z. Xing and X. Yang, *Nat. Commun.*, 2019, **10**, 3899.
32 G. Li, Q. Xu, W. Shi, C. Fu, L. Jiao, M. E. Kamminga, M. Yu, H. Tüysüz, N. Kumar, V. Süß, R. Saha, A. K. Srivastava, S. Wirth, G. Auffermann, J. Gooth, S. Parkin, Y. Sun, E. Liu and C. Felser, *Sci. Adv.*, 2019, **5**, eaaw9867.
33 S. Sun, Y. Zhang, X. Shi, W. Sun, C. Felser, W. Li and G. Li, *Adv. Mater.*, 2024, **36**, 2312524.
34 Y. Zhang, Y. Wang, W. Sun, D. Ma, J. Ma, J. Rao, Q. Xu, J. Huo, J. Liu and G. Li, *Adv. Mater. Interfaces*, 2023, **10**, 2300279.
35 A. Moysiadou, S. Lee, C. Hsu, H. M. Chen and X. Hu, *J. Am. Chem. Soc.*, 2020, **142**, 11901–11914.
36 M. Pan, H. Feng, Z. Zhang, M. Gao, L. Lei, D. Wang, G. Li, J. Huo and J. Wang, *J. Mater. Chem. A*, 2024, **12**, 15334–15342.
37 N. C. Hurtig, A. P. Gysi, S. E. Smith-Schmitz and D. Harlov, *Dalton Trans.*, 2024, **53**, 9964–9978.
38 H. Xu, K. Yue, L. Song, H. Zhang, H. Zhu, Z. Zhang and G. Li, *Angew. Chem., Int. Ed.*, 2024, **63**, e202412025.
39 C. Yang, O. Fontaine, J. Tarascon and A. Grimaud, *Angew. Chem., Int. Ed.*, 2017, **56**, 8652–8656.
40 L. Gu, C. Li, J. Zhao, L. Xie, J. Wu, Q. Ren and G. Li, *J. Mater. Chem. A*, 2021, **9**, 13279–13287.
41 A. Gaur, J. Sharma and V. Bagchi, *ChemCatChem*, 2024, **16**, e202301438.

 This journal is © The Royal Society of Chemistry 2025